

Frequency Comb Shaping Through Staggered Phase Flux in Fast Gain Lasers

Diego Picicocchi^{1,†,*}, Alexander Dikopoltsev^{1,†,*}, Ina Heckelmann¹,
Mattias Beck¹, Giacomo Scalari¹, Jerome Faist^{*1}

¹*Institute for Quantum Electronics and Quantum Center, ETH Zürich, 8093 Zürich, Switzerland.*

*Corresponding authors. Email: dpicicocchi@phys.ethz.ch, adikopoltsev@phys.ethz.ch, jfaist@phys.ethz.ch

Abstract

Optical frequency-comb devices are essential in telecommunications, sensing, and metrology. Yet, precise in-situ control of their spectral envelope remains challenging. We demonstrate a spectral shaping technique leveraging path-dependent phase engineering in the synthetic lattice of cavity modes in a ring-shaped laser with ultrafast gain recovery. By modulating the laser at its repetition rate and twice this frequency, we create a 1D triangular ladder with a staggered phase flux, which breaks time-reversal symmetry. This enables continuous tuning of a strong central lobe across the full bandwidth of our Quantum Cascade Laser frequency comb at 1340cm^{-1} . Our method offers unprecedented spectral control at the light generation stage in any fast gain active device, opening new opportunities in waveform engineering for ranging, data transmission, and sensing.

Main

Over the past decades, Optical Frequency Combs (OFCs) have driven innovation across science and engineering (1), enabling breakthroughs in spectroscopy (2), metrology (3) and microwave synthesis (4). The development of compact platforms(5), such as microcombs and mode-locked lasers, has significantly reduced the size and power consumption, enabling portable applications and foundry compatibility (6). These advancements unlock dense data transmission (7), parallelized photonic neural networks (8) and on chip sensing (9), all within a miniaturized form factor.

Shaping the spectrum of OFCs is valuable across multiple fields. In spectroscopy, spectral reconfiguration of the source allows to tune the response function and removes complexity from the detection system, enabling single-pixel spectroscopy (10). For applications using comb lines as orthogonal sources, such as dense optical communication (11) or ranging (12), frequency-domain synthesis enables power management and channel navigation. In quantum information, spectral control improves atomic transition control (13), superconducting qubit driving (14) and frequency-bin encoding (15). Existing methods that shape the output spectrum of a device rely on dispersion-engineering (16, 17) or on-chip filters (18, 19). Still, portable systems would benefit from in-situ shaping, which reduces complexity and allows for spectral reconfiguration within the light source during operation.

Due to their perfect equal spacing, the modes of an OFC can be viewed as sites in a -synthetic- frequency lattice (20), enabling the exploration of fundamental phenomena such as the Quantum Hall effect (21), Bloch oscillations (22, 23), topological insulation (24), gauge potentials (25) and non-Abelian fields (26). Lattices in synthetic dimensions offer key advantages over real space systems, such as tuneable long-range interactions (27) and increased dimensionality (28–30), holding the key to precise and robust spectral control. While applications in efficient quantum simulations (31), optical isolation (20) and mode-locking (32) have recently emerged, effective implementations that exploit this flexibility to shape OFC spectra in active devices remain scarce (22, 33).

We propose and demonstrate an efficient in-situ method for shaping OFC spectra through path-phase-dependent synthetic lattices in ring lasers, enabled by fast gain recovery (Fig. 1A). By modulating the laser cavity at its resonances, f_{rep} and $2f_{\text{rep}}$, we induce nearest- and next-nearest neighbor coupling along the

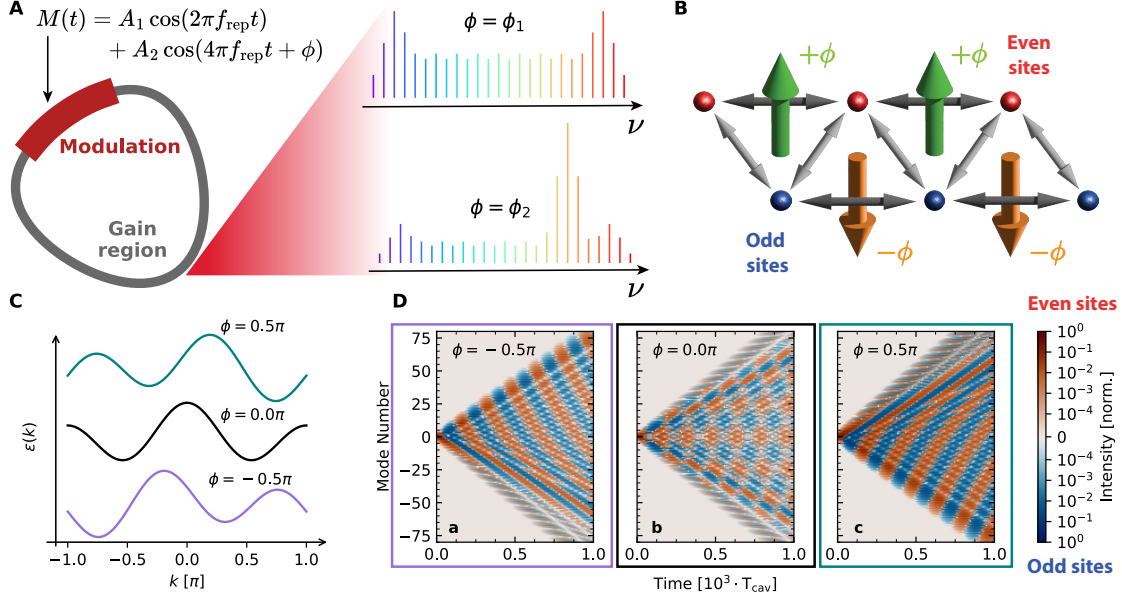


Figure 1: Engineering Path-Phase Dependence of Synthetic Lattices in Fast Gain Lasers. (A) Dual-tone modulation of a ring cavity laser, shaping the spectrum using the phase shift ϕ . (B) The modes of the ring cavity form a synthetic lattice with a triangular ladder geometry with staggered phase flux. The light (dark) gray arrow show coupling induced by f_{rep} ($2f_{\text{rep}}$) modulation, and even (odd) modes are shown on the top (bottom). The green and orange arrows show the direction of the phase accumulated by hopping in a triangular plaquette. (C) The band structure of the synthetic lattice, dictated by the modulation in the cavity’s real space (the synthetic lattice’s reciprocal space). (D) Time evolution of a single site excitation in triangular ladder lattices with different path dependent phases ($\phi = 0, \pm\pi/2$). When $\phi \neq 0, \pi$, time-reversal symmetry is broken, causing directional energy transfer between odd and even sub-lattices.

synthetic frequency lattice of cavity modes, forming a triangular ladder geometry (Fig. 1B). The relative phase between these couplings introduces a staggered path-dependent phase that breaks time-reversal symmetry, altering the band structure and energy transfer between lattice sites. Fast gain recovery ensures quasi-constant intensity, maximizing the overlap between the temporally extended field and the modulation. This makes the spectral dynamics and steady state exceptionally sensitive to the engineered lattice structure and the path-dependent phase, enabling dynamic spectral shaping at the light generation stage.

Our demonstration, based on the continuous wave operation of fast gain devices, clarifies why most pulsed OFC sources have yet to fully leverage the potential of synthetic dimensions for spectral control. While electro-optic combs (34) achieve flexible spectral shaping by coupling OFC modes through amplitude and phase modulation, they do not operate in a resonant regime. Therefore, the nonlinear process requires long modulation paths and significant power (35). Our technique enables on-the-fly spectral tuning directly within portable OFC sources, leveraging fast gain (36–40) and its coherent liquid flow dynamics (23), opening new possibilities in ranging, spectroscopy and communications.

Winding in synthetic lattices

We consider a laser with a circular cavity (41, 42), whose modes define a one-dimensional lattice along the synthetic frequency dimension. The modes are coupled by radio-frequency modulation of the injected current at harmonics of the cavity resonance frequency, Nf_{rep} . This electrical signal is translated to phase modulation through the linewidth enhancement factor (43), enabling coupling between N^{th} -neighbors along the lattice of the cavity modes. Here, we introduce a path-dependent coupling phase by combining radio-frequency (RF) modulations at f_{rep} and $2f_{\text{rep}}$, and controlling their amplitudes, A_1, A_2 and their relative phase, ϕ (Fig. 1A).

Using this modulation scheme, we induce nearest-neighbor (NN) and next-nearest-neighbor (NNN) cou-

plings (Fig. 1B) in the synthetic lattice (44). The onsite potential is quadratic and complex, and is determined by the dispersion, β , gain curvature, g_c , and cavity wavevector K . Consequently, the linear part of this system can be described using the following Hamiltonian

$$H = \sum_m (D - iG)m^2 b_m b_m^\dagger + \sum_m C_{\text{NN}} \cdot b_{m+1}^\dagger b_m + C_{\text{NNN}} e^{i\phi} \cdot b_{m+2}^\dagger b_m + \text{h.c.} \quad (1)$$

where b_m^\dagger, b_m are the creation and annihilation operators of a photon in mode $m \in \mathbb{Z}$, with $D = \beta K^2/2$ and $G = g_c K^2/2$. $C_{\text{NN}} = A_1/2$ and $C_{\text{NNN}} = A_2/2$ are the amplitudes of the NN and NNN coupling coefficients, respectively (S1). The relative phase ϕ (Fig. 1C) between the two modulation components is translated to the phase factor $e^{i\phi}$ for the coupling term C_{NNN} , and cannot be trivially removed. This Hamiltonian describes the structure of a lattice with a triangular ladder geometry, which is shown in Fig. 1B, with even and odd modes appearing on different sides. The phase between the two coupling terms introduces a staggered phase flux, analogous to an Aharonov-Bohm phase (45), through each triangular lattice plaquette. This phase flux can be visualized considering a closed hopping path with a defined orientation (clockwise or counterclockwise), composed of two nearest-neighbor hops and one next-nearest-neighbor hop closing the path, resulting in an accumulated non-trivial phase of $+\phi$ and $-\phi$ (Fig. 1B).

The phase flux effectively breaks the time-reversal symmetry of the system (44). Specifically, the modulation at f_{rep} and $2f_{\text{rep}}$, which is defined in the real space of the system (Fig. 1A), causes coupling along the synthetic frequency dimension (Fig. 1B), i.e. in the system's reciprocal space. The band structure of this synthetic lattice is defined in its reciprocal space, which in this case is again the real space of the cavity. Interestingly, this implies that the modulation directly corresponds to the band structure (Fig. 1C), given by

$$\varepsilon(k) = 2C_{\text{NN}} \cos(k) + 2C_{\text{NNN}} \cos(2k + \phi), \quad (2)$$

where k is a coordinate in the cavity space. The breaking of the time-reversal symmetry is reflected in the fact that as $\phi \neq 0, \pi$ the band structure $\varepsilon(k)$ is no longer symmetric around $k = 0$ (Fig. 1C), and impacts the population dynamics of the lattice. This is illustrated in Fig. 1D in the absence of both the quadratic potential and nonlinear term, starting from the occupation of a single lattice site. Fig. 1D shows the dynamics of the lattice population for trivial phase $\phi = 0$ and nontrivial phases $\phi = \pm 0.5\pi$. Within the regime of broken time-reversal symmetry, it is possible to observe a periodic and chiral flow of intensity between the even (red) and odd (blue) sub-lattices, whose winding direction follows the phase ϕ . Fig. 1D also shows the same dynamics for a symmetric band structure with a trivial phase $\phi = 0$, showing symmetric dynamics between the even and odd sub-lattices.

Enabling spectral control with fast gain

The phase-dependent dynamics are imprinted on the steady-state of our mode-locked laser source. The ring-shaped semiconductor laser is based on a Quantum Cascade Laser (QCL) (41) active medium with an ultrafast gain recovery time, < 1 ps, much shorter than the cavity round-trip time, which is in the order of tens of picoseconds (40). Such gain adds a non-Hermitian nonlinear term to the field dynamics. This is included in the equations for the evolution of the mode amplitudes B_m as

$$i \frac{dB_m}{dt} = (D - iG)m^2 B_m + C_{\text{NN}} \cdot (B_{m+1} + B_{m-1}) + C_{\text{NNN}} \cdot (e^{i\phi} B_{m+2} + e^{-i\phi} B_{m-2}) + F_{\text{NL}}(I(t)), \quad (3)$$

where $I(t)$ is the time-dependent intensity of the electromagnetic field. The solutions of this nonlinear equation provide the steady states for the lattice occupation, which directly correspond to the intensity in each mode at frequency ν_m , i.e. the spectrum of the device $S(\nu_m) = |B_m|^2$.

The role of the fast gain nonlinear term F_{NL} is to induce a non-Hermitian long range coupling between the modes that forces quasi-constant intensity in the cavity. We note that our system naturally fulfills the condition of starting at a single site, since the gain causes spontaneous symmetry breaking of the lasing direction, while low surface roughness enables single mode lasing (39). When the phase modulation is applied, the coupling transfers population to other sites of the synthetic lattice, while the fast-gain constrains the amplitudes and phases to keep the total intensity quasi-constant in time (39). The resulting intracavity intensity, being approximately constant with time, extends over the whole cavity cycle and overlaps maximally

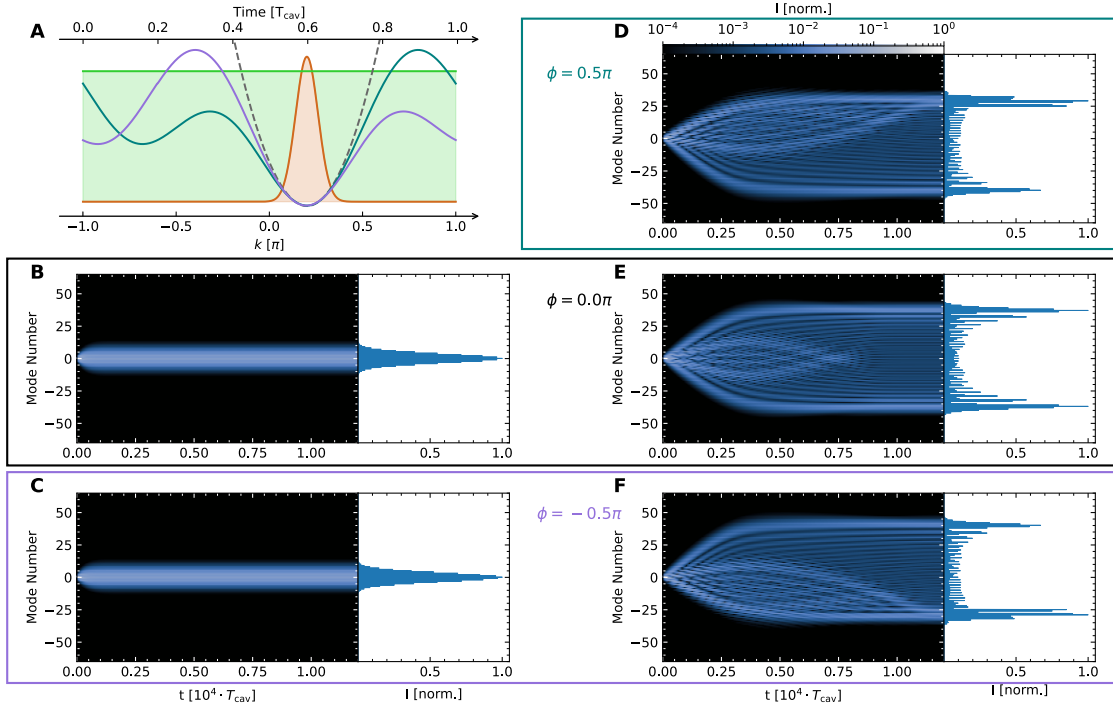


Figure 2: Impact of the Phase and Nonlinearity on Lattice Dynamics. (A) Comparison of pulsed and extended signals under modulation. Fast gain ensures a quasi-continuous intracavity intensity that overlaps with the modulation profile throughout the whole round-trip. In contrast, systems with pulsed intensities only sample the local shape of the modulation, which here is a parabolic minimum. This explains why pulsed signal are only weakly manipulated by phase modulation. (B), (C) Time evolution of the spectral state for slow gain, supporting pulsed lasing. We observe that for two different modulation signals, the resulting steady state is insensitive to the phase ϕ . (D-F) The fast gain system show a significant response to the change in ϕ . By probing the full modulation, both the dynamics and the steady state show the chiral lattice dynamics, making the final spectrum sensitive to the phase ϕ .

with the modulation signal, as shown in Fig. 2A. This makes the intracavity field sensitive to the functional shape of the modulation across the full period. This is in contrast to a pulsed intracavity field that will only probe a local part of the modulation shape, here approximately parabolic, being insensitive to its symmetry properties for the rest of the period. Therefore, the addition of the fast-gain term is crucial for enabling sensitivity to the underlying synthetic lattice.

To show this impact, we compare dynamics in the fast gain medium to media in which the gain recovery is slow, where the losses from saturation are acting on the averaged signal, i.e. $g(t) = g_0 / (1 + \langle I(t) \rangle / I_{\text{sat}})$. Fig. 2B and C (see S2 for details) show the time evolution of the spectrum of slow gain ring lasers using modulations with the same amplitudes for the f_{rep} and $2f_{\text{rep}}$ components and two different values of $\phi = 0, \pi/2$. Even though the two phases produce modulation profiles which differ with respect to their time-reversal symmetry properties, the profile around the minimum is almost unaffected. In both cases, the evolution starts from a single mode, corresponding to the occupation of a single lattice site. At time $t = 0$, the modulation is switched on and the modes begin to proliferate. With slow gain, the stabilization is governed by dissipation, induced by gain curvature. This process is also known as active mode locking, and it typically leads to a spectrally narrow Gaussian state (46) (Fig. 2B, C). In contrast, the continuous intensity enforced by the fast gain makes the system sensitive to the full modulation profile. As a consequence, the chiral flow of energy in the underlying lattice (shown in Fig. 1D) is imprinted in the nonlinear dynamics, as shown in Fig. 2D-F for three values of the phase, $\phi = 0, \pm\pi/2$. The effect of the nontrivial phase is translated both in the initial dynamics and in the steady state reached by means of the fast gain, as is particularly clear for the cases in which the symmetry is broken ($\phi = \pm\pi/2$). This control of the steady state through the engineering of the

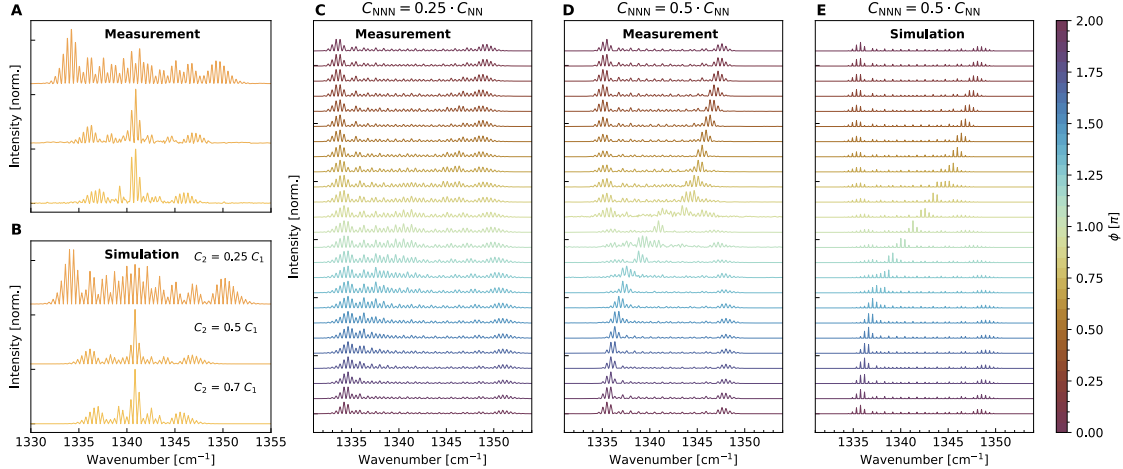


Figure 3: Spectral Shaping with Phase. (A), (B) Effect of changing the amplitudes of the signals at f_{rep} and $2f_{\text{rep}}$ for a fixed phase $\phi = \pi$. As the amplitude of the $2f_{\text{rep}}$ component increases, a peak in the central region of the spectrum appear. (C), (D) Effect of the phase, ϕ , between the modulation signals at f_{rep} and $2f_{\text{rep}}$ on the steady-state optical spectrum of the fast gain laser. As ϕ is increasing, the peak from (A), (B) is changing its central position to higher frequencies in the spectrum, until it winds back. The injection components have fixed values of their relative amplitudes, with $C_{\text{NNN}} = 0.25C_{\text{NN}}$ and $C_{\text{NNN}} = 0.5C_{\text{NN}}$, respectively. (E) Simulation of the steady state of the same amplitude modulation values in (D).

geometry of a synthetic lattice -the sensitivity to which is enabled by the fast gain- is what makes in-situ spectral control possible.

Demonstration of spectral shaping

The ring-shaped QCL has a cavity length of $L_c \approx 7.1\text{mm}$, corresponding to a resonance frequency of $f_{\text{rep}} = 12.534\text{GHz}$. When operated without any modulation, the device is in single mode regime, emitting at $\nu_0 = 1341\text{cm}^{-1}$ ($\approx 7.46\mu\text{m}$). We demonstrate the control over the spectrum by manipulating the synthetic lattice with two synchronized radio frequency current modulation signals at f_{rep} and $2f_{\text{rep}} = 25.068\text{GHz}$, injected into the semiconductor fast-gain ring laser device, and translated to phase modulation through the gain. For each value of the phase between the two modulation frequencies, ϕ , we allow the laser to reach the steady state spectrum and measure it with a Fourier Transform InfraRed (FTIR) spectrometer (details in S3 and Fig. 4).

Fig. 3A and B show the effect of the amplitude of the two modulation components on the steady state spectrum for a fixed value of $\phi = \pi$ in both experimental measurements and numerical simulations. An increase in the amplitude A_2 (or NNN coupling, C_{NNN}) leads to the progressive appearance of a peak in the central region of the spectrum, demonstrating that tuning the amplitudes of the coupling enables the observation of localized features in the spectrum. Notably, the achieved bandwidth ($\approx 15\text{cm}^{-1}$) is constrained by the response of the electrical connections at $2f_{\text{rep}}$ and does not represent an intrinsic limitation of the driving scheme (details in S4 and Fig. 5).

Next, we show in Fig. 3C and D that the spectral features can be manipulated by changing the phase across the $[0, 2\pi]$ range, demonstrated for two different values of $A_{1,2}$. The resulting steady state spectral shapes contain peaks that scan the entirety of the available bandwidth, allowing for controllable intensity transfer across the whole spectral range. We also note that, as the ratio between NN and NNN coupling decreases, the intensity transfer in the spectrum becomes progressively smoother, illustrating the combined effect of shaping using the two degrees of freedom of relative amplitudes and phase. The agreement with the numerical simulation (Fig. 3E) confirms the prediction that the effect of time-reversal symmetry breaking driven by the lattice's phase flux directly affects the output spectrum of the device, while the winding of the phase is imprinted on the scan of the steady state spectra.

Concluding remarks

We have demonstrated a spectral shaping scheme based on the engineering of a triangular synthetic lattice with a staggered phase flux, producing configurations that break time-reversal symmetry. This is done by modulating the current of a mid-IR QCL at the cavity’s FSR and its second harmonic. The system’s responsivity to the path-phase dependent lattice structure is enabled by the fast gain recovery of the semiconductor device. The fast gain forces a quasi-constant field intensity over the entire optical cycle, allowing control over the spectral envelope by tuning the relative amplitude and phase of the two modulation components. This method is broadly applicable beyond QCLs, extending to any medium with instantaneous incoherent pumping dynamics that support Quantum Walk Comb operation (39). For instance, this spectral shaping method could be adapted to devices operating in the L and C bands through fast interband processes (40) or incoherent second harmonic pumping (47).

The fast gain enables the nonlinear system to access new steady states that inherit the properties of the underlying synthetic lattice. A natural extension of this work is the implementation of phase-dependent modulation schemes at higher harmonics (30, 48) to introduce N th-neighbor coupling. This would provide additional degrees of freedom for spectral shaping by translating fine-grained RF domain signal engineering into the optical domain, paving the way to a new generation of optical synthesis techniques. Such capabilities could reduce the complexity of spectral measurement systems by shifting manipulations from interferometric detection to direct light source control. Furthermore, this technique could be applied to pulse compression by dispersion compensation (49), transferring the flexibility of spectral tuning to pulse shaping. Together, these perspectives underscore the potential of multi-frequency modulated fast-gain laser as tunable and customizable light sources.

Acknowledgments

Funding: This work was supported by the following: MIRAQLS: Staatssekretariat für Bildung, Forschung und Innovation SBFI (22.00182) in collaboration with EU (grant Agreement 101070700); Swiss National Science Foundation (212735); Innosuisse: Innovation Project 52899.1 IP-ENG (Agreement Number 2155008433 “High yield QCL Combs”); ETH Fellowship program: (22-1 FEL-46) (to A.D.)

Author contributions: D.P. and A.D. performed the characterizations, developed the models, performed the numerical simulations and wrote the original draft. A.D. and I.H. conceptualized the idea. D.P. wrote the Supplementary Materials. I.H. processed the devices. M.B. grew the QCL wafer and consulted in the fabrication. A.D., G.S., and J.F. acquired the funding, administrated, and supervised the project. All authors contributed to the interpretation of the results and the review and editing of the draft.

Competing interests: There are no competing interests to declare.

Data and materials availability: Data that support the findings of this article are available in the ETH Research Collection (50).

References

1. S. A. Diddams, K. Vahala, T. Udem, *Science* **369**, Publisher: American Association for the Advancement of Science, eaay3676, (2024; <https://www.science.org/doi/full/10.1126/science.aay3676>) (July 2020).
2. N. Picqué, T. W. Hänsch, en, *Nature Photonics* **13**, Publisher: Nature Publishing Group, 146–157, ISSN: 1749-4893, (2024; <https://www.nature.com/articles/s41566-018-0347-5>) (Mar. 2019).
3. T. Udem, R. Holzwarth, T. W. Hänsch, en, *Nature* **416**, Publisher: Nature Publishing Group, 233–237, ISSN: 1476-4687, (2024; <https://www.nature.com/articles/416233a>) (Mar. 2002).
4. T. M. Fortier *et al.*, en, *Nature Photonics* **5**, Publisher: Nature Publishing Group, 425–429, ISSN: 1749-4893, (2024; <https://www.nature.com/articles/nphoton.2011.121>) (July 2011).
5. A. L. Gaeta, M. Lipson, T. J. Kippenberg, en, *Nature Photonics* **13**, Publisher: Nature Publishing Group, 158–169, ISSN: 1749-4893, (2024; <https://www.nature.com/articles/s41566-019-0358-x>) (Mar. 2019).
6. L. Chang, S. Liu, J. E. Bowers, en, *Nature Photonics* **16**, Publisher: Nature Publishing Group, 95–108, ISSN: 1749-4893, (2024; <https://www.nature.com/articles/s41566-021-00945-1>) (Feb. 2022).
7. Y. Okawachi, B. Y. Kim, M. Lipson, A. L. Gaeta, EN, *Optica* **10**, Publisher: Optica Publishing Group, 977–995, ISSN: 2334-2536, (2024; <https://opg.optica.org/optica/abstract.cfm?uri=optica-10-8-977>) (Aug. 2023).
8. S. Biasi *et al.*, *Intelligent Computing* **3**, Publisher: American Association for the Advancement of Science, 0067, (2024; <https://spj.science.org/doi/10.34133/icomputing.0067>) (Jan. 2024).
9. K. Han *et al.*, EN, *Optica* **11**, Publisher: Optica Publishing Group, 392–398, ISSN: 2334-2536, (2025; <https://opg.optica.org/optica/abstract.cfm?uri=optica-11-3-392>) (Mar. 2024).
10. H. H. Yoon *et al.*, *Science* **378**, Publisher: American Association for the Advancement of Science, 296–299, (2025; <https://www.science.org/doi/10.1126/science.add8544>) (Oct. 2022).
11. B. Corcoran *et al.*, en, *Nature Communications* **11**, Publisher: Nature Publishing Group, 2568, ISSN: 2041-1723, (2025; <https://www.nature.com/articles/s41467-020-16265-x>) (May 2020).
12. Y.-S. Jang, S. Eom, J. Park, J. Jin, *Optics & Laser Technology* **170**, 110324, ISSN: 0030-3992, (2024; <https://www.sciencedirect.com/science/article/pii/S0030399223012173>) (Mar. 2024).
13. Y. Ma *et al.*, EN, *Optics Express* **28**, Publisher: Optica Publishing Group, 17171–17187, ISSN: 1094-4087, (2025; <https://opg.optica.org/oe/abstract.cfm?uri=oe-28-12-17171>) (June 2020).
14. D. Lee *et al.*, *APL Photonics* **8**, 086115, ISSN: 2378-0967, (2025; <https://doi.org/10.1063/5.0157003>) (Aug. 2023).
15. H.-H. Lu, M. Liscidini, A. L. Gaeta, A. M. Weiner, J. M. Lukens, EN, *Optica* **10**, Publisher: Optica Publishing Group, 1655–1671, ISSN: 2334-2536, (2025; <https://opg.optica.org/optica/abstract.cfm?uri=optica-10-12-1655>) (Dec. 2023).
16. G. Moille, X. Lu, J. Stone, D. Westly, K. Srinivasan, en, *Communications Physics* **6**, Publisher: Nature Publishing Group, 1–11, ISSN: 2399-3650, (2024; <https://www.nature.com/articles/s42005-023-01253-6>) (June 2023).
17. M. Roy, Z. Xiao, C. Dong, S. Addamane, D. Burghoff, EN, *Optica* **11**, Publisher: Optica Publishing Group, 1094–1102, ISSN: 2334-2536, (2024; <https://opg.optica.org/optica/abstract.cfm?uri=optica-11-8-1094>) (Aug. 2024).
18. H. Shu *et al.*, en, *Nature* **605**, Publisher: Nature Publishing Group, 457–463, ISSN: 1476-4687, (2024; <https://www.nature.com/articles/s41586-022-04579-3>) (May 2022).
19. L. M. Cohen *et al.*, en, *Nature Communications* **15**, Publisher: Nature Publishing Group, 7878, ISSN: 2041-1723, (2024; <https://www.nature.com/articles/s41467-024-52051-9>) (Sept. 2024).
20. T. Ozawa, H. M. Price, N. Goldman, O. Zilberberg, I. Carusotto, *Physical Review A* **93**, Publisher: American Physical Society, 043827, ISSN: 24699934, (<https://journals.aps.org/pr/abstract/10.1103/PhysRevA.93.043827>) (Apr. 2016).

21. T. Ozawa, I. Carusotto, *Physical Review Letters* **112**, Publisher: American Physical Society, 133902, (2024; <https://link.aps.org/doi/10.1103/PhysRevLett.112.133902>) (Apr. 2014).
22. N. Englebert *et al.*, *Nature Physics* **2023**, Publisher: Nature Publishing Group, 1–8, ISSN: 1745-2481, (<https://www.nature.com/articles/s41567-023-02005-7>) (Apr. 2023).
23. A. Dikopoltsev *et al.*, *Quench dynamics of Wannier-Stark states in an active synthetic photonic lattice*, en, May 2024, (2024; <https://arxiv.org/abs/2405.04774v1>).
24. E. Lustig *et al.*, en, *Nature* **567**, Publisher: Nature Publishing Group, 356–360, ISSN: 1476-4687, (2025; <https://www.nature.com/articles/s41586-019-0943-7>) (Mar. 2019).
25. L. Yuan, Y. Shi, S. Fan, en, *Optics Letters* **41**, 741, ISSN: 0146-9592, 1539-4794, (2023; <https://opg.optica.org/abstract.cfm?URI=ol-41-4-741>) (Feb. 2016).
26. D. Cheng *et al.*, en, *Nature* **637**, Publisher: Nature Publishing Group, 52–56, ISSN: 1476-4687, (2025; <https://www.nature.com/articles/s41586-024-08259-2>) (Jan. 2025).
27. L. J. Maczewsky *et al.*, en, *Nature Photonics* **14**, Publisher: Nature Publishing Group, 76–81, ISSN: 1749-4893, (2024; <https://www.nature.com/articles/s41566-019-0562-8>) (Feb. 2020).
28. E. Lustig *et al.*, en, *Nature* **609**, Publisher: Nature Publishing Group, 931–935, ISSN: 1476-4687, (2025; <https://www.nature.com/articles/s41586-022-05129-7>) (Sept. 2022).
29. Y. Hu, C. Reimer, A. Shams-Ansari, M. Zhang, M. Loncar, EN, *Optica* **7**, Publisher: Optica Publishing Group, 1189–1194, ISSN: 2334-2536, (2025; <https://opg.optica.org/optica/abstract.cfm?uri=optica-7-9-1189>) (Sept. 2020).
30. A. Schwartz, B. Fischer, EN, *Optics Express* **21**, Publisher: Optica Publishing Group, 6196–6204, ISSN: 1094-4087, (2025; <https://opg.optica.org/oe/abstract.cfm?uri=oe-21-5-6196>) (Mar. 2013).
31. U. A. Javid *et al.*, *Nature Photonics* **2023**, Publisher: Nature Publishing Group, 1–8, ISSN: 1749-4893, (<https://www.nature.com/articles/s41566-023-01236-7>) (June 2023).
32. Z. Yang *et al.*, *Physical Review X* **10**, Publisher: American Physical Society, 011059, (2025; <https://link.aps.org/doi/10.1103/PhysRevX.10.011059>) (Mar. 2020).
33. A. Tusnin, A. Tikan, K. Komagata, T. J. Kippenberg, en, *Communications Physics* **6**, Publisher: Nature Publishing Group, 1–10, ISSN: 2399-3650, (2025; <https://www.nature.com/articles/s42005-023-01438-z>) (Nov. 2023).
34. A. Parriaux, K. Hammani, G. Millot, EN, *Advances in Optics and Photonics* **12**, Publisher: Optica Publishing Group, 223–287, ISSN: 1943-8206, (2024; <https://opg.optica.org/aop/abstract.cfm?uri=aop-12-1-223>) (Mar. 2020).
35. J. B. Khurgin, en, *Laser & Photonics Reviews* **18**, _eprint: <https://onlinelibrary.wiley.com/doi/pdf/10.1002/lpor.202300836>, ISSN: 1863-8899, (2024; <https://onlinelibrary.wiley.com/doi/abs/10.1002/lpor.202300836>) (2024).
36. A. Hugi, G. Villares, S. Blaser, H. C. Liu, J. Faist, *Nature* **492**, 229–233, ISSN: 00280836 (Dec. 2012).
37. L. A. Sterczewski, C. Frez, S. Frouhar, D. Burghoff, M. Bagheri, *APL Photonics* **5**, 076111, ISSN: 2378-0967, (2025; <https://doi.org/10.1063/5.0009761>) (July 2020).
38. B. Dong *et al.*, en, *Light: Science & Applications* **12**, Publisher: Nature Publishing Group, 182, ISSN: 2047-7538, (2025; <https://www.nature.com/articles/s41377-023-01225-z>) (July 2023).
39. I. Heckelmann *et al.*, *Science* **382**, Publisher: American Association for the Advancement of Science, 434–438, (2023; <https://www.science.org/doi/10.1126/science.adj3858>) (Oct. 2023).
40. B. Marzban *et al.*, *A Quantum Walk Comb Source at Telecommunication Wavelengths*, arXiv:2411.08280 [physics], Nov. 2024, (2025; <http://arxiv.org/abs/2411.08280>).
41. B. Meng *et al.*, *Nature Photonics* **2021 16:2 16**, Publisher: Nature Publishing Group, 142–147, ISSN: 1749-4893, (<https://www.nature.com/articles/s41566-021-00927-3>) (Dec. 2021).
42. N. Opačak *et al.*, en, *Nature* **625**, Publisher: Nature Publishing Group, 685–690, ISSN: 1476-4687, (2025; <https://www.nature.com/articles/s41586-023-06915-7>) (Jan. 2024).

43. N. Opačak *et al.*, EN, *Optica* **8**, Publisher: Optica Publishing Group, 1227–1230, ISSN: 2334-2536, (2024; <https://opg.optica.org/optica/abstract.cfm?uri=optica-8-9-1227>) (Sept. 2021).
44. A. Dutt *et al.*, *Nature Communications* **10**, 3122, ISSN: 2041-1723, (<https://doi.org/10.1038/s41467-019-11117-9>) (July 2019).
45. Y. Aharonov, D. Bohm, *Physical Review* **115**, Publisher: American Physical Society, 485–491, (2025; <https://link.aps.org/doi/10.1103/PhysRev.115.485>) (Aug. 1959).
46. H. A. Haus, *IEEE Journal of Quantum Electronics* **11**, 323–330, ISSN: 15581713 (1975).
47. H. S. Stokowski *et al.*, en, *Nature* **627**, Publisher: Nature Publishing Group, 95–100, ISSN: 1476-4687, (2024; <https://www.nature.com/articles/s41586-024-07071-2>) (Mar. 2024).
48. D. Cheng, E. Lustig, K. Wang, S. Fan, en, *Light: Science & Applications* **12**, Publisher: Nature Publishing Group, 158, ISSN: 2047-7538, (2024; <https://www.nature.com/articles/s41377-023-01196-1>) (June 2023).
49. P. Täscher *et al.*, en, *Nature Photonics* **15**, Publisher: Nature Publishing Group, 919–924, ISSN: 1749-4893, (2024; <https://www.nature.com/articles/s41566-021-00894-9>) (Dec. 2021).
50. D. Piciocchi, A. Dikopoltsev, *Frequency comb shaping through staggered phase flux in fast gain lasers*, en, Accepted: 2025-03-12T06:58:42Z, Mar. 2025, (2025; <https://www.research-collection.ethz.ch/handle/20.500.11850/726502>).

Methods

S1 - Derivation of Tight-Binding Model

Here, we discuss how the tight-binding model used throughout this work can be obtained from an equation for the electromagnetic field under RF modulation at f_{rep} and $2f_{\text{rep}}$.

We start from the current density, written as in the main text

$$J(t) = J_0 + A_1 \cdot \cos(2\pi f_{\text{rep}}t) + A_2 \cdot \cos(4\pi f_{\text{rep}}t + \phi).$$

Here, J_0 is the DC bias current of the device, $A_{1,2}$ are the amplitudes of the current modulation, f_{rep} is the cavity free-spectral range.

We start from the cGLE-like equation describing the field propagation, in a reference frame co-propagating with the initial single mode (23, 39):

$$i\dot{E} = i \left[g_0 \left(1 - \frac{I(t)}{I_{\text{sat}}} \right) - \alpha \right] E + \left(\frac{i}{2}g_c - \frac{\beta}{2} \right) \nabla^2 E + \theta(t) \cdot [2C_{\text{NN}} \cos(Kz) + 2C_{\text{NNN}} \cos(2Kz + \phi)] E.$$

Here, g_0 is the unsaturated gain factor, I and I_{sat} are the field intensity and saturation intensity, α is the total loss, g_c is the gain curvature, β is the dispersion and K the wavevector corresponding to the resonance frequency. The amplitude modulation is converted to phase modulation by the linewidth enhancement factor (LEF) and $2C_{\text{NN,NNN}}$ are the phase modulation coefficients corresponding to the two components.

Now, we assume the RF modulation to be turned on at $t = 0$ and restrict ourselves to $t \geq 0$. Considering only the linear and energy-conserving part, the equation becomes

$$\dot{E} = \left(i\frac{\beta}{2} + \frac{g_c}{2} \right) \nabla^2 E - i \cdot 2 [C_{\text{NN}} \cos(Kz) + C_{\text{NNN}} \cos(2Kz + \phi)] \cdot E.$$

Now, we write the field as an expansion containing all equally spaced cavity modes $E(t) = \sum_n B_n(t)e^{-inKz}$ and insert it in the previous expression

$$\begin{aligned} \sum_n \dot{B}_n e^{-inKz} &= \left(i\frac{\beta}{2} + \frac{g_c}{2} \right) \sum_n (-inK)^2 B_n e^{-inKz} - 2iC_{\text{NN}} \cos(Kz) \sum_n B_n e^{-inKz} \\ &\quad - 2iC_{\text{NNN}} \cos(2Kz + \phi) \sum_n B_n e^{-inKz} \\ &= -i \frac{(\beta - ig_c)K^2}{2} \sum_n n^2 B_n e^{-inKz} - iC_{\text{NN}} \sum_n B_n \left[e^{-i(n-1)Kz} + e^{-i(n+1)Kz} \right] \\ &\quad - iC_{\text{NNN}} \sum_n B_n \left[e^{-i(n-2)Kz+i\phi} + e^{-i(n+2)Kz-i\phi} \right]. \end{aligned}$$

Now, multiplying by e^{imKz} , integrating over z and defining $D = (\beta - ig_c)K^2/2$, we find

$$\dot{B}_m = -iDm^2 B_m - iC_{\text{NN}} (B_{m+1} + B_{m-1}) - iC_{\text{NNN}} (B_{m+2}e^{-i\phi} + B_{m-2}e^{i\phi}).$$

Introducing the creation and annihilation operators for photons in mode m , b_m and b_m^\dagger , the Hamiltonian can be written as:

$$H = \sum_m D \cdot m^2 b_m b_m^\dagger + C_{\text{NN}} (b_{m-1}^\dagger b_m + b_{m+1}^\dagger b_m) + C_{\text{NNN}} (b_{m-2}^\dagger b_m e^{i\phi} + b_{m+2}^\dagger b_m e^{-i\phi}).$$

Now, we can proceed with the derivation of the band structure. For the sake of notation simplicity, we write the Hamiltonian with the Dirac notation. We omit the dispersion and gain curvature terms, whose role is to provide a boundary for the population of modes far from the bottom of the potential

$$H = \sum_m C_{\text{NN}} (|m-1\rangle \langle m| + |m+1\rangle \langle a_m|) + C_{\text{NNN}} (|m-2\rangle \langle m| e^{i\phi} + |m+2\rangle \langle m| e^{-i\phi}).$$

Now, we introduce the plane wave decomposition for the eigenstates $|m\rangle$ of the uncoupled system:

$$|m\rangle = \frac{1}{\sqrt{N}} \sum_k e^{imk} |k\rangle \langle k| \quad (4)$$

and insert it in the previous equation. This results in

$$\begin{aligned} H &= \sum_m \left\{ C_{\text{NN}} \left(\frac{1}{\sqrt{N}} \sum_k e^{i(m-1)k} |k\rangle \langle k| \frac{1}{\sqrt{N}} \sum_q e^{-imq} |q\rangle \langle q| \right. \right. \\ &\quad \left. \left. + \frac{1}{\sqrt{N}} \sum_k e^{i(m+1)k} |k\rangle \langle k| \frac{1}{\sqrt{N}} \sum_q e^{-imq} |q\rangle \langle q| \right) \right. \\ &\quad \left. + C_{\text{NNN}} \left(\frac{1}{\sqrt{N}} \sum_k e^{i(m-2)k} |k\rangle \langle k| \frac{1}{\sqrt{N}} \sum_q e^{-imq} |q\rangle \langle q| \right. \right. \\ &\quad \left. \left. + \frac{1}{\sqrt{N}} \sum_k e^{i(m+2)k} |k\rangle \langle k| \frac{1}{\sqrt{N}} \sum_q e^{-imq} |q\rangle \langle q| \right) \right\} \\ &= \frac{1}{N} \sum_k |k\rangle \langle k| \sum_q |q\rangle \langle q| \sum_m e^{im(k-q)} [C_{\text{NN}}(e^{ik} + e^{-ik}) + C_{\text{NNN}}(e^{2ik} + e^{-2ik})] \\ &= \sum_k |k\rangle \langle k| \sum_q |q\rangle \langle q| \delta_{k,q} [C_{\text{NN}}(e^{ik} + e^{-ik}) + C_{\text{NNN}}(e^{2ik} + e^{-2ik})] \\ &= \sum_k |k\rangle \langle k| [2C_{\text{NN}} \cos(K) + 2C_{\text{NNN}} \cos(2k + \phi)] \end{aligned} \quad (5)$$

This being a diagonal Hamiltonian, the dispersion relation is simply:

$$\varepsilon(k) = 2C_{\text{NN}} \cos(k) + 2C_{\text{NNN}} \cos(2k + \phi) \quad (6)$$

S2 - Numerical Simulations

The numerical simulations shown in Fig. 2, illustrating the lattice dynamics and the impact of fast gain, were performed by solving Equation 3. We solve the equation

$$i \frac{d\psi}{dt} = H\psi + F_{\text{NL}}(I(t)), \quad (7)$$

using an explicit Runge-Kutta algorithm of order 5. Here, we describe how the operators H and F_{NL} are calculated. $\psi = [\psi_{N/2}, \dots, \psi_m, \dots, \psi_{N/2}]^T$ represents the complex spectrum, i.e. the complex amplitude in each of the N lattice sites.

The linear part of the system is described by a the square matrix

$$H_{i,j} = D \cdot \delta_{i,j} \cdot m^2 + C_{\text{NN}} \cdot \delta_{i,j\pm 1} + C_{\text{NNN}} e^{\pm i\phi} \cdot \delta_{i,j\pm 2}, \quad (8)$$

which implements the tight-binding model illustrated in the previous section. This matrix operator acts in the basis of the cavity modes, i.e. in the synthetic space of our lattice. Therefore, it is directly applied to the state ψ by matrix multiplication at each time-step.

The effect of gain saturation, which depends on the intensity $I(t)$, is implemented in the time domain. First, the intensity is computed by Fourier transforming the field and taking the square modulus: $I(t) = |\mathcal{F}^{-1}[\psi](t)|^2$. Then, depending on the nature of the gain (slow or fast), the saturation term is computed and transformed back to the cavity mode basis

$$G_{\text{sat,fast}} = \mathcal{F} \left[g_0 \left(1 - \frac{I(t)}{I_{\text{sat}}} \right) \psi \right], \quad G_{\text{sat,slow}} = \mathcal{F} \left[g_0 \left(1 - \frac{\langle I(t) \rangle}{I_{\text{sat}}} \right) \psi \right]. \quad (9)$$

Here g_0 is the unsaturated gain factor and I_{sat} the saturation intensity.

For more practical matching to the physical parameters of the device, like dispersion, gain and gain curvature, the simulations shown in Fig. 3 are performed using the complex Ginzburg-Landau equation described in the previous section (S1). The equation is solved using the split-step method (39). Therefore, the evolution is split into two operators. The first one, containing terms related to dispersion and gain curvature, is diagonal in the frequency domain and therefore is applied on the spectrum, obtained from the intracavity field upon application of the Fourier transform. The second one, containing the term due to the gain saturation and modulation, is diagonal in the time domain and is applied on the field directly. This is, in practice, identical to what is done when solving the lattice equation. The time step for the simulation is chosen to be small enough for a stable convergence of the simulation, while the duration is chosen to be long enough to ensure that the steady state is reached.

S3 - Experimental Apparatus

Fig. 4 shows the experimental apparatus used for dual-tone modulation of the laser. The Quantum Cascade Laser is operated at a DC bias current of 1A, generated with a QCL2000 source by Wavelength Electronics. The two Radio Frequency (RF) modulation tones are produced by two separate generators (SMF 100A and SMB 100A by Rhode and Schwarz), synchronized via a 10MHz line. The generator used for the $2f_{\text{rep}}$ component is operated at an output power of 27dBm, while the power used in the $1f_{\text{rep}}$ generator is chosen according to the desired relative modulation amplitude, eventually with the use of an amplifier. The spectrum is acquired with a Fourier Transform InfraRed (FTIR, Bruker Vertex 80), using an external Mercury-Cadmium-Telluride (MCT) detector (by Kolmar Technologies).

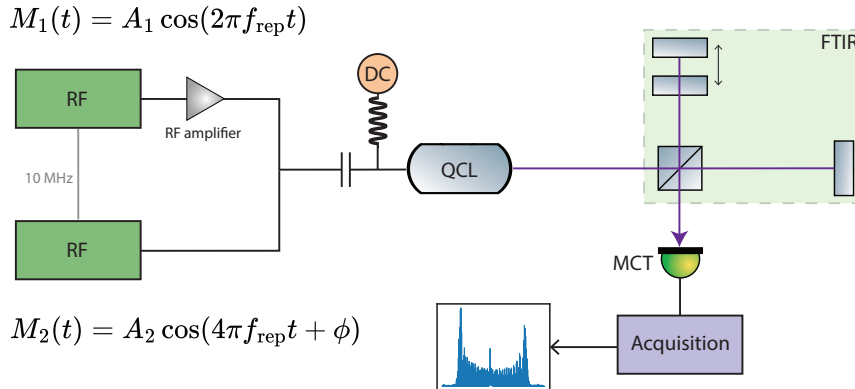


Figure 4: Experimental apparatus used for the dual-tone injection. The QCL is injected with two tones generated by synchronized radio-frequency generators. The emitted light is then analyzed with an FTIR to retrieve the spectrum as a function of the phase between the two tones.

S4 - Bandwidth limits

In the experimental conditions tested in this work, the device shows a bandwidth of approximately 15cm^{-1} , much smaller than the one predicted for these devices with similar injection power when using only the tone at f_{rep} (39). Here, we demonstrate that this is largely due to the size of the device, pushing the $2f_{\text{rep}}$ tone at $\approx 25\text{GHz}$, where the electrical response to the modulation is substantially weakened. One effect is the electrical response of the active region, which behaves as an RC low-pass filter. Its RC product was calculated as

$$RC = \varepsilon_0 \varepsilon_r R_d, \quad (10)$$

where $\varepsilon_0\varepsilon_r$ is the dielectric permittivity of the active region and R_d is the normalized differential resistance of the device. Considering the differential resistance of the device around our working point, we obtain an RC product of $\approx 5\text{ps}$ and cutoff frequency of $f_{3\text{dB,AR}} \approx 33\text{GHz}$. Therefore, the device itself would in principle respond efficiently to the tone at $2f_{\text{rep}}$. However, the $2f_{\text{rep}}$ component will be attenuated by the response of the electrical connector used to connect the RF source to the PCB board on which the laser is mounted, which is optimized up to 18GHz . This additional attenuation affects only the $2f_{\text{rep}}$ tone. Additionally, the PCB board for the RF driving itself was optimized for injection at f_{rep} . We assume the same cutoff frequency of 18GHz for the PCB board as well, in order to estimate the attenuation. The full electrical response function, accounting for the effects described above, is shown in Fig. 5A. The attenuation of the $2f_{\text{rep}}$ tone is overall $\approx 15\text{dB}$ larger than it is for the f_{rep} one.

Driving our device with a certain power at f_{rep} or $2f_{\text{rep}}$ will give the same comb bandwidth. Therefore, considering the attenuation difference and the fact that we use a power of 27dBm at $2f_{\text{rep}}$, we expect to achieve the same comb bandwidth when using $\approx 12\text{dBm}$ at f_{rep} . In Fig.5B, we report the comparison with a spectrum obtained when driving at f_{rep} with a power $\approx 10\text{dBm}$, showing matching of the bandwidth. The residual attenuation can be ascribed to electrical components not accounted for in the computed transfer function, such as the short wires used to connect the PCB board to the laser's top contact.

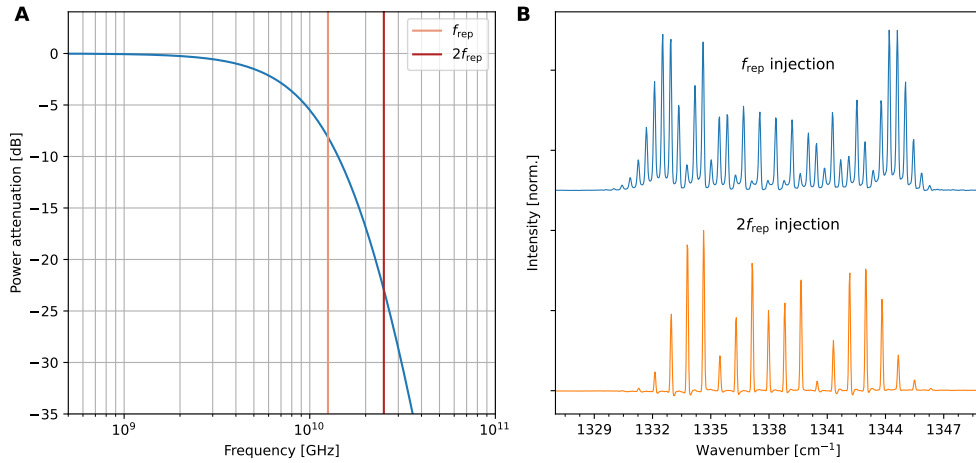


Figure 5: Electrical response of the circuit and bandwidth. (A) Electrical response of the circuit. (B) Spectra using only the f_{rep} tone at $\approx 10\text{dBm}$ and the $2f_{\text{rep}}$ one at $\approx 27\text{dBm}$, in good agreement with the $\approx 15\text{dB}$ relative attenuation between the two tones.